

# Off-equilibrium reactivity of boron-enriched metal diboride surfaces in electro-reduction conditions

Zisheng Zhang<sup>†,‡</sup> and Frank Abild-Pedersen<sup>\*,†</sup>

<sup>†</sup>SUNCAT Center for Interface Science and Catalysis, SLAC National Accelerator Laboratory, Menlo Park, CA 94025, United States

<sup>‡</sup>Department of Chemical Engineering, Stanford University, Stanford, California 94305, United States

E-mail: abild@slac.stanford.edu

## Abstract

Boron-based material, featuring B-dependent reactivity and diverse phases, is emerging as a promising catalyst system. However, catalytic mechanism on many borides remains poorly understood due to complex surface reconstructions under reaction conditions. Here, we investigate the MoB<sub>2</sub> surface in conditions of hydrogen evolution reaction in acidic media, using grand canonical global optimization, grand canonical density functional theory, *ab initio* molecular dynamics, free energy surface sampling, and an analytical model for electrochemical barrier evaluation. We propose a boron enrichment strategy to tune the surface reactivity of the hexagonal face of MoB<sub>2</sub>. We reveal the dynamic nature of the B-enriched surface under H coverage and kinetic trapping of the system in the metastable regime, with an extensive examination on the deactivation pathways. The metastable center B site on B-enriched surfaces, featuring buckled-up configuration and an usual relaxation effect, is found to be highly active towards HER via Volmer-Heyrovsky mechanism. This work demonstrates how off-equilibrium behaviors can arise from the interplay between adsorbate coverage and

surface reconstruction on a seemingly simple surface, and we present a theoretical framework and computational workflows to address them, along with other realistic complexities, in kinetics simulations.

## Introduction

Boron, a metalloid element with three valence electrons, is known to form unusual delocalized skeletal bonding<sup>1</sup> that defy the conventional view of covalency, such as the octet rule, which has been stimulating the development of modern chemical bonding theories.<sup>2</sup> Its unique electronic structure gives rise to great structural diversity in bulk and two-dimensional allotropes,<sup>3,4</sup> surface terminations,<sup>5</sup> as well as pure boron clusters.<sup>6</sup> When doped with transition metal, the boron clusters exhibit even more exotic structures and chemical bonding.<sup>7,8</sup> As a result, boron was considered as "arguably the most complex element in the periodic table".<sup>9</sup>

Such structural and electronic complexities persist in boron compounds. Metal borides, with particularly diverse stoichiometries and polymorphs, has hence emerged as a promising material system with highly tunable chemical and physical properties with broad applications, including superhardness,<sup>10</sup> superconductivity,<sup>11</sup> magnetism,<sup>12</sup> corrosion resistance,<sup>13</sup> thermoelectrics,<sup>14</sup> and so on.

Non-precious transition metal borides, meriting low cost and tunable properties, have been synthesized in nano-crystal form<sup>15–17</sup> and extensively tested for various electrocatalytic reactions,<sup>18,19</sup> as alternatives to the noble metal-based catalysts. Hydrogen evolution reaction (HER) on non-precious metal borides,<sup>20</sup> in particular, exhibits intriguing boron-dependency: the electrocatalytic activity depends heavily on the richness and structural arrangements of the boron content (ionic, chains, rings, graphene- and phosphene-like layers, or even cages), rather than the metal content.<sup>21,22</sup> The boron arrangement can be highly fluxional in some borides, inducing spontaneous disordering thermally.<sup>23</sup> As a result, atomistic understanding of the HER active sites' structure and reactivity in realistic conditions has still been lacking.

The challenge in modeling boron-based catalysts lies in the strong oxygen and hydrogen affinity of boron, which results in various types of off-stoichiometric surface reconstructions during operation. Under oxidative dehydrogenation conditions, the boron content on the boride surface can get partially hydroxylated/oxidized and form an amorphous overlayer solely responsible for the catalysis,<sup>24–27</sup> with metal-independent reaction mechanisms.<sup>28</sup> Under reducing or H-rich conditions, the surface boron content can get reversibly hydrogenated to form layered hydrogen boride<sup>29</sup> or borophane<sup>30</sup> with dramatically altered chemical reactivity.<sup>31,32</sup> Extra boron content on surface, as residual from synthesis, can also lead to complex and nontrivial surface reconstruction.<sup>33,34</sup> In electrocatalytic conditions, the system further complicates from interplay between surface restructuring, varying electrode potential and solvent/electrolyte organization.<sup>35–38</sup> Hence, it is necessary to consider potential structural rearrangements as well as the realistic aspects of the electrochemical interface under relevant conditions when studying catalysis on borides.

In this work, we revisit MoB<sub>2</sub>, the most HER-active undoped non-precious metal boride according to experimental reports.<sup>20</sup> Since such high activity originates in the graphene-like hexagonal layered arrangement of boron content within MoB<sub>2</sub>, we focus on the boron-terminated (001) facet, the hexagonal face. Grand canonical (GC) global optimizations are performed at density functional theory (DFT) level to sample the surface reconstruction under boron rich or deficient synthetic conditions, and surface configurations under varying coverage of reaction intermediate H. *Ab initio* thermodynamics predicts that the B-enriched surface should undergo a major deactivating reconstruction under higher H coverages. However, computed barriers prove that the major reconstruction is kinetically unfavorable, and that the surface boron would be trapped in its pristine configuration although it would become metastable thermodynamically at higher H coverages. To simulate the HER activity, we perform GC-DFT and *ab initio* molecular dynamics (AIMD) simulations to obtain the accessible coverage state in the HER-relevant potential window, and the coverage-dependent spatial distribution of near-surface water. We also discover strong adsorption-dependent

reshaping of a specific center-atop site and how its relative time scale to HER elementary steps would influence the HER kinetics.

## Results and discussion

### Tunable surface structure through B-enrichment

In a typical diboride, the B-terminated (001) facet features an exposed B sheet with graphene-like honeycomb structure, which we treat as the reference stoichiometry and refer as the hexagonal face in the following. The hexagonal boron sheets are anionic and intercalated by layers of Mo cations in between (Figure S3). Inspired by the great structural diversity of 2-dimensional borophene and planar boron clusters, we make our first attempt to access such diversity by introducing B surplus or deficit into the hexagonal face. Experimentally, this can be achieved by controlling the amount of boron element or reagent either during the synthesis process or through an extra surface treatment step on the prepared catalyst.

To account for the potential rearrangement of surface boron, we performed global optimization minima search of the surface structure at DFT level (Supplementary Note S1). 727 unique surface phases are discovered in a wide stoichiometric range, from -1/2 to +1 monolayer (ML) of B coverage, with the structures of the global minimum (GM) surface phase of each stoichiometry shown in Figure S8. Here the monolayer B coverage is defined with respect to the number of  $B_6$  hexagons. By calculating the approximated grand canonical (GC) free energy with respect to B,  $\Omega_B$ , of the sampled structures, we can evaluate the relative thermodynamic stability of the structures with different B coverage,  $\mu_B$ .

$$\Omega_B \approx E_{n_B} - E_{\text{bare}} - n_B \mu_B \quad (1)$$

Here  $E$ ,  $n_B$ , and  $\mu_B$  are the electronic energy, number of extra B atoms *per* simulation box, and chemical potential of B, respectively, with the bare surface being the reference.

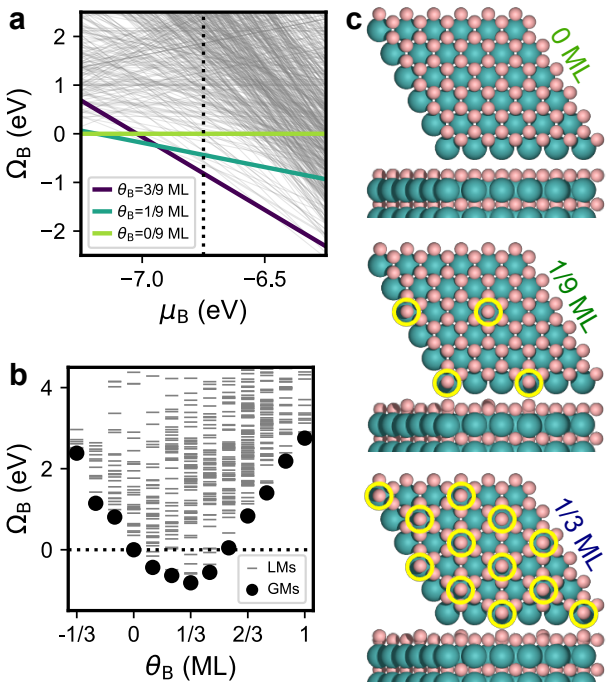


Figure 1: *Ab initio* thermodynamics of boron-enriched hexagonal face of MoB<sub>2</sub>. (a) Surface phase diagram of the MoB<sub>2</sub> surface with varying coverage of extra surface boron as a function of chemical potential of B, from grand canonical global optimization sampling. The dotted line marks the chemical potential relevant to B enrichment. (b) Grand canonical free energy of the sampled surface phases with respect to B, at the chemical potential relevant to B enrichment. (c) Top and front views of the structures of the three surface phases (B<sub>0</sub>, B<sub>1/9</sub>, and B<sub>1/3</sub>) that can be prepared by boron-enrichment. The extra boron atoms are marked by yellow circles. Color code of atoms: Mo – blue, B – pink.

This expression allows us to establish the surface phase diagram of MoB<sub>2</sub> hexagonal face as a function of  $\mu_B$ . In Figure 1a, each line represent a unique surface phase, and the different stoichiometries lead to different response of  $\Omega_B$  to varying  $\mu_B$ . To better visualize the B coverage-dependent trend of thermodynamic stability of the surface phases, we can slice the phase diagram at any specific value of  $\mu_B$ , such as -6.75 eV (pure elemental boron), as in Figure 1b, revealing a stability convex hull of the GM surface phases.

Because the synthetic conditions are typically at high temperature, and there is no slow in-bulk diffusion of B involved in the surface rearrangement itself, it is safe to assume that the system can fully equilibrate and access the thermodynamically most stable surface phase during preparation. Therefore, we will focus only on the global minimum (GM) surface phase

of each stoichiometry in the rest of this section. With the  $\mu_B$  of pure elemental boron being the upper limit of the  $\mu_B$  in the preparation process, we only consider the surface phases that can be stabilized within the range of  $\mu_B < -6.75$  eV as synthetically viable. We then exclude the B-deficient surface phases due to high chemical instability of the exposed edge defects (Figure S8) and the energy penalty for breaking of the hexagonal lattice as can be seen in  $\theta_B < 0$  segment of the GM convex hull in Figure 1b. This narrows our scope down to three pristine or B-enriched surface phases in Figure 1c, referred to as  $B_0$ ,  $B_{1/9}$ , and  $B_{1/3}$ .

The hexagonal skeleton of the pristine surface  $B_0$  stays almost unchanged in all of the three surface phases, with the additional B content merely filling in the centers of the hexagons in a slightly buckled-up configuration. Moreover, the additional center B atoms tend to repel each other within the hexagonal B lattice instead of aggregate to form a "belt". These behaviors are quite different from the case of 2-dimensional B allotropes and main group metal diborides.<sup>3,23</sup> The preservation of the hexagonal skeleton on MoB<sub>2</sub> is likely due to the stronger interaction between B and transition metal outcompeting the fluxionality of B-B networks, leading to the dominance of the Mo lattice over the arrangement of surface B. The center B atoms, which introduce significant local strain within the sheet, hence tend to not stay adjacent to each other but be evenly distributed over the hexagonal lattice. The distribution of center B in  $B_{1/9}$  and  $B_{1/3}$  specifically matches the symmetry of the hexagonal lattice, resulting in strong stabilization as is reflected by the inaccessibility of  $B_{2/9}$  in Figure 1a and the sharp bottom of the GM convex hull in Figure 1b. Experimentally, we believe that terminations with  $\theta_B$  between 1/9 and 1/3 ML should consist of a mixture of local regions of the  $B_{1/9}$  and  $B_{1/3}$  phases.

## Reactivity of the B-enriched surfaces under H coverage

Having identified the three B-rich surface phases that can potentially be prepared by B-enriching treatment, we move on to examine their electrochemical reactivity. In this work, we investigate the HER in highly acidic media (pH=0) where H is the only type of adsorbate,

and no water splitting is involved. This avoids the otherwise complication of hydroxylation or borate formation in alkaline media or at oxidizing potentials (Figure S2), which we plan to address in a later study.

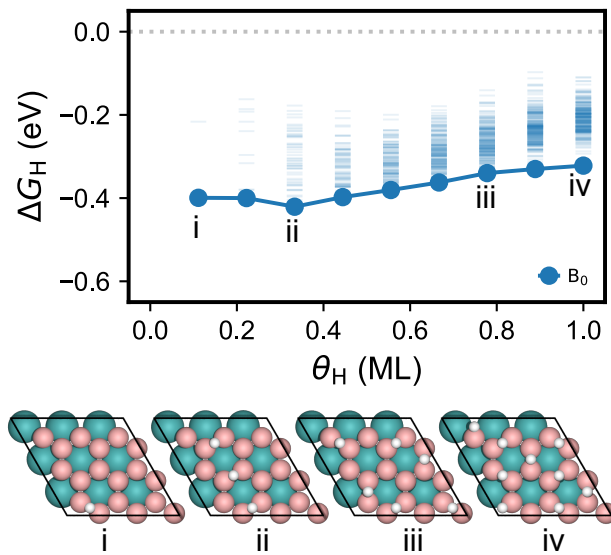


Figure 2: Adsorption free energetics of H on pristine  $B_0$  hexagonal face of  $MoB_2$  under varying H coverage. The bar and circle markers represent all sampled structures and the most stable structure of each H coverage, respectively. Representative structures are shown under the plot and labeled in Roman numerals. Color code of atoms: Mo – blue, B – pink, H – white.

We firstly study the pristine phase  $B_0$  to establish a reference for comparison with the other two B-enriched phases. The covalent and molecular nature of B-H bond and the B network necessitates a non-mean-field approach to adsorbate coverage effects, i.e., explicitly finding all HER-relevant adsorption configurations. Grand canonical genetic algorithm (GCGA) is used to perform GC minima search of  $B_0$  under varying H coverage (Supplementary Note S1), with the grand canonical free energy with respect to H,  $\Omega_H$ , as the search target:

$$\Omega_H \approx E_{n_H} - E_{\text{bare}} - n_H \mu_H \quad (2)$$

where the  $\mu_H$  is a function of reaction conditions such as pH and electrode potential  $U$ . The  $\delta E$  terms denote the thermal correction terms to the free energy related to the H adsorption,

including the zero point energy, constant pressure heat capacity, and vibrational entropy.

$$\mu_H = \frac{1}{2}E_{H_2}^{\text{gas}} + (\delta E_H^{\text{gas}} - \delta E_H^{\text{ads}}) - \ln(10)k_B T pH - |e|U_{\text{SHE}} \quad (3)$$

In total, we sampled 1,665 unique catalyst states from multiple independent GCGA searches. The H adsorption free energies,  $\Delta G_H$ , of all the GCGA-sampled catalyst states up to 1 ML H coverage are plotted in Figure 2, with notable GM structures shown below. The monolayer H coverage is defined as the highest possible H coverage without causing disintegration of the hexagonal skeleton.  $B_0$  binds H quite strongly, with the  $\Delta G_H$  ranging from -0.4 eV to -0.3 eV as the H coverage increases. This over-binding behavior is comparable to that of Mo and Re metals.<sup>39</sup>

In the whole HER-relevant coverage regime, H always prefers to adsorb onto the bridge site (Figure S16) over the B-B edge of the hexagon units (Figure S9). This is a typical 3-center-2-electron ( $3c-2e$ ) bonding mode as is characterized by the curvature of the bond path ( $151.7^\circ$ ) and a small positive Laplacian (0.016) at the bond critical point (Figure S7 and Table 1). The bridge H appears as highly hydridic with a Bader charge of about  $-0.5|e|$ , accompanying with significant electron transfer from the B that it binds to (Figure S3), and this trend persists in the whole coverage range (S4). At 1/3 ML H coverage, the H adsorbates prefer to occupy the two parallel edges of the hexagons and align along a straight line. At higher coverages, they tend to spread out and adopt an alternating occupied-empty-occupied-empty pattern within each hexagon. Having two H atoms on adjacent bridge sites is highly energetically unfavorable, as the electron density on the two B atoms hosting the H is depleted (Figure S3), reducing their ability to accommodate another H. The H arrangement also has significant symmetry stabilization effect, leading to a small spike in H adsorption strength at 1/3 and 1 ML.

For the  $B_{1/9}$  phase, we conduct GCGA searches similarly, obtaining 2,197 unique catalyst states in total. The  $\Delta G_H$  of all the GCGA-sampled catalyst states up to 1 ML H coverage

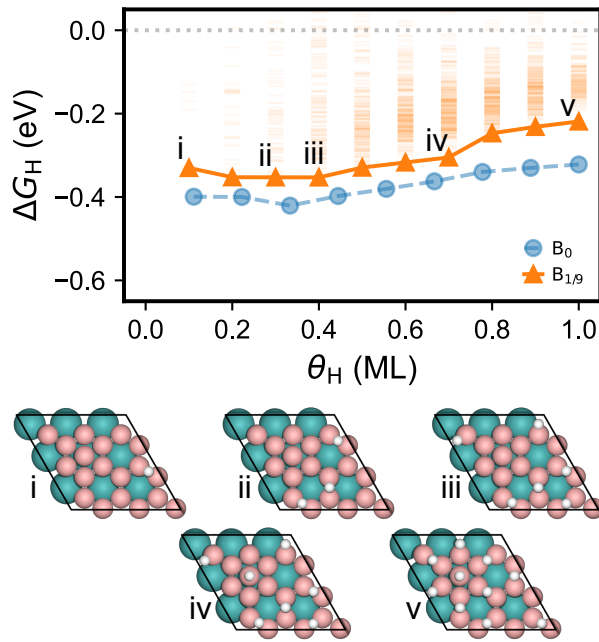


Figure 3: Adsorption free energetics of H on the  $B_{1/9}$ -enriched hexagonal termination of  $\text{MoB}_2$  under varying H coverage. The bar and circle markers represent all sampled structures and the most stable structure of each H coverage, respectively. Representative structures are shown under the plot and labeled in Roman numerals. Color code of atoms: Mo – blue, B – pink, H – white.

are plotted in Figure 3, with notable GM structures shown below. Comparing to  $B_0$ , the  $B_{1/9}$  phase binds H weaker by about 0.1 eV in the whole coverage range, with energetics similar to Ni and Co metals. The weakening of H binding can be attributed to the multi-center bonding formed within the  $B_7$  unit (center B and its host  $B_6$  unit), a typical aromatic motif, as is characterized by the strong electron delocalization above it (Figure S5). This disables the  $B_7$  unit from forming bridge binding modes and slightly consumes the electron density within the extended conjugated system of the hexagonal sheet (Figure S3 and S4), overall weakening H binding on surface B.

The center B also breaks the symmetry of the hexagonal lattice, creating a distribution of non-equivalent and non-degenerate surface sites. At low coverage, the H adsorbates prefer to occupy bridge sites that are distant from the  $B_7$  unit (Figure S16). As H coverage increases, H continues to fill the region not adjacent to the  $B_7$  unit, until it saturates at 2/5 ML.

The next incoming H binds onto the center B in an atop  $\sigma$  mode, which weakens the bond between the center B and its host  $B_6$  unit (Figure S5), leading to elevation by about 0.4 Å (Figure S15). This also partially weakens the conjugation within the  $B_7$  (Figure S6) and activates the host  $B_6$  unit (Figure S7 and Table S1), enabling H binding on the peripheral bridges sites of the  $B_7$  unit at higher coverages. This leads to significant charge transfer from the center B to both its atop H and the host  $B_6$  unit (Figure S3). Similar to the case of  $B_0$  phase, the H-covered  $B_{1/9}$  phase exhibits a repulsive interaction among H adsorbates, with each surface B atom accommodating at most one H and each  $B_6$  unit accomodating up to 3 H.

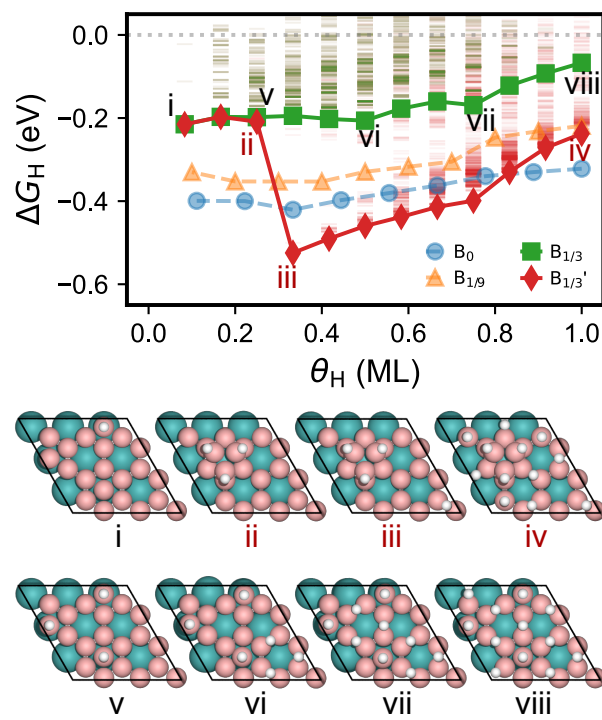


Figure 4: Adsorption free energetics of H on the  $B_{1/3}$ -enriched hexagonal termination of  $\text{MoB}_2$  under varying H coverage. The bar and circle markers represent all sampled structures and the most stable structure of each H coverage, respectively. Representative structures are shown under the plot and labeled in Roman numerals. Color code of atoms: Mo – blue, B – pink, H – white.

Then we move on to the  $B_{1/3}$  phase which has a higher extra surface B content, featuring alternating  $B_6$  and  $B_7$  units across the hexagonal lattice. Again we performed GCGA global

optimizations to search for the minima structure under varying coverage. However, this time the searches takes a much larger amount of sampling to converge, resulting in 6,149 unique catalyst states in the final ensemble.

The  $\Delta G_H$  of all the GCGA-sampled catalyst states up to 1 ML H coverage are plotted in Figure 3, with notable GM structures shown below. At lower coverages, H prefers to bind atop the center B sites rather than the bridge sites as on  $B_0$  and  $B_{1/9}$  phases (Figure S16). This change arises from the higher surface density of center B, which depletes the free valence electrons across the hexagonal lattice and deactivate the bridge B sites between the  $B_7$  units. Furthermore, since the lattice constants are largely dictated by the  $\text{MoB}_2$  bulk, an increased density of center B induces significant strain within the sheet. This strain leads to greater structural buckling of the  $B_7$  units (Figure S15), making them more susceptible to H binding. Consequently, the center-atop  $B^*\text{H}$  emerges as the most favorable adsorption mode. Overall,  $B_{1/3}$  still binds H weaker than the  $B_0$  and  $B_{1/9}$  phases, promising better HER thermodynamics.

However, beyond 1/4 ML coverage, the H binding gets surprisingly stronger, exhibiting a cliff-like drop in  $\Delta G_H$  to about  $-0.5$  eV. Similarly, we also observed a dramatic drop in grand canonical free energy during the GCGA search (Figure S12). This quite unphysical behavior turns out to be the result of a major surface reconstruction (Figure 4ii-iv): the center B atoms can alternatively aggregate into a  $B_3$  trimer and reside over a  $B_6$  unit, rearranging into a face-centered hemi-icosahedral motif. This reconstruction is only energetically competitive after all additional B are covered by H. Interestingly, upon the clustering of center  $B^*\text{H}$ , the freed  $B_6$  units are activated and can afford much stronger H binding as compared to those in the unreconstructed  $B_{1/3}$  phase. This makes the reconstructed phase, referred to as  $B_{1/3}'$ , a much worse HER electrocatalyst. In addition, the strong stabilization of H-covered  $B_3$  trimer creates effectively a thermodynamic sink (Figure S20), trapping H indefinitely while deactivating the entire surface for HER.

## Coverage-dependent kinetics of the deactivation pathways

The clustering and deactivation behavior of the extra surface B content is quite reminiscent of the sintering and ripening of nanoparticles in heterogeneous catalysis: while the thermodynamic fate of the system is to aggregate into an inactive monolith, kinetic barriers may slow down or even prevent this process. This prompts us to look into the kinetics of reconstruction.

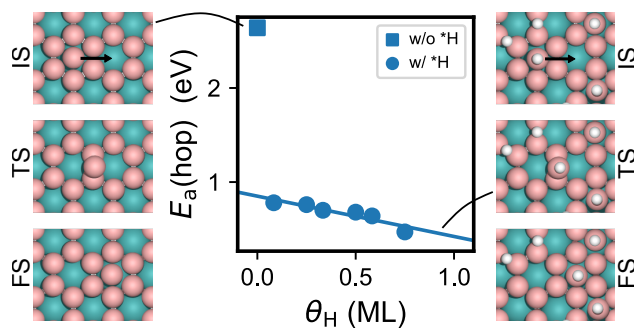


Figure 5: Activation barriers of center B hopping on  $B_{1/3}$  surface under varying H coverage. Representative structures of the initial, transition, and final states are shown next to the plot. Color code of atoms: Mo – blue, B – pink, H – white.

To initiate the reconstruction, the center B atom must leave its original host  $B_6$  unit and migrate across the surface. Initially, we consider an in-plane rearrangement mechanism, but it turns out to be kinetically unfavorable with high barriers of about 1.5 eV (Figure S17). This is contrary to the case of  $MgB_2$ ,<sup>23</sup> likely due to the stronger Mo–B interaction (than the mostly ionic Mg–B) which "protects" the intactness of the hexagonal lattice. Additionally, the center B must migrate together with its atop H adsorbate as a single entity.

Hence, we consider a hopping mechanism, where a center B hops to its adjacent  $B_6$  unit *via* the shared B–B edge. To compute the activation barriers,  $E_a$ , we sample the potential energy surface (PES) of the center B hopping at varying H coverages and then locate the minimum energy path (MEP) and transition state (TS) by the string method (Supplementary Note S2). The computed hopping barriers and the representative structures along the hopping coordinates are shown in Figure 5. If there is no atop H on the center B, the

hopping barrier would be extremely high, at about 3 eV, making it kinetically impossible. However, just by adding an atop H onto the center B, its hopping barrier is reduced to below 1 eV. Such changes is due to the significant weakening of the the B-B bond between the center B and its hist B<sub>6</sub> by forming an atop B-H bond, demonstrating the covalent and molecular nature of the boron sheet, in stark contrast with metallic surfaces. Adding more H to the peripheral bridges sites on the surface would further lower the barrier, and the barrier reduction correlates with the H coverage. At high H coverages, the hopping barrier can be reduced to below 0.5 eV, which means that the hopping of center B\*H is quite viable at room temperature.

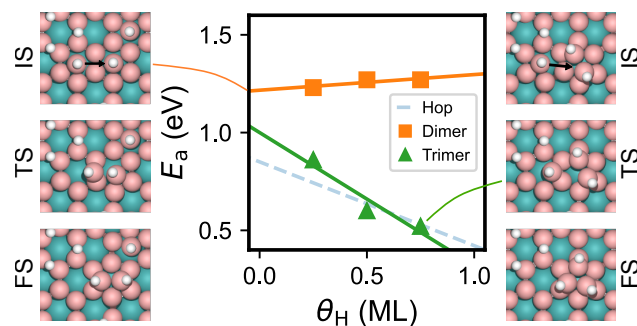


Figure 6: Activation barriers of center B dimerization and trimerization on B<sub>1/3</sub> surface under varying H coverage. Representative structures of the initial, transition, and final states are shown next to the plot. Color code of atoms: Mo – blue, B – pink, H – white.

As the center B\*H hops around, they may meet and associate over a B<sub>6</sub> unit. This requires a starting configuration where the two center B\*H are on two adjacent B<sub>6</sub> units. Firstly, we consider the process where one of the B\*H (donor) migrates toward the other (acceptor) to form a dimer (Figure 6). This dimerization turns out to be neither thermodynamically nor kinetically feasible, with the barrier of about 1.25 eV in the whole coverage range. This can be rationalized by examining the TS structure: while the bridging configuration of the donor BH closely resembles that of the hopping TS, the acceptor BH must partially detach from its host B<sub>6</sub> unit to accommodate the donor B\*H and rearrange into a B<sub>6</sub>-supported dimer, incurring a significant energy penalty. We then consider the subsequent trimerization process where another donor B\*H migrates to associate with an adjacent dimer. Trimerization is found to

be highly exothermic, with a strong negative correlation between the trimerization barrier and H coverage. This trend can be attributed to the milder structural rearrangement required on the dimer side at the TS, causing the donor side to dictate the barrier. Consequently, the coverage dependence of the hopping and dimerization barriers is quite similar, both decreasing to below 0.5 eV at higher H coverage. However, since dimer formation is not feasible, trimerization will not occur in the first place. As a result, the system shall be kinetically trapped in a metastable regime where center B\*H species can hop around but never associate, let alone aggregate into clusters.

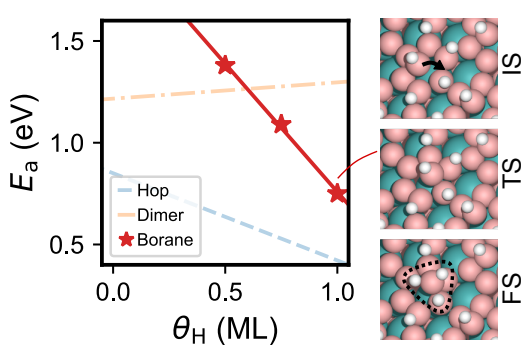


Figure 7: Activation barriers of borane formation from center B on  $B_{1/3}$  surface under varying H coverage. Representative structures of the initial, transition, and final states are shown next to the plot. Color code of atoms: Mo – blue, B – pink, H – white.

Since thermodynamics predict that boron content decomposes into borane under acidic electro-reduction conditions (Figure S2), which leads to loss of surface B content, we also compute the barriers for borane-like species formation at different H coverages. We find that borane can only form when a center B\*H migrates toward a B–B edge with two H adsorbates on adjacent bridge sites. As the migrating B\*H bridges over the B–B edge, it interacts with the two adjacent H adsorbates and uptake them to form a  $BH_3$  borane which can readily desorb. The borane formation barrier decreases significantly with increasing H coverage, exhibiting a strong negative correlation. At very high H coverage, the barrier is reduced to approximately 0.75 eV, which remains a relatively slow process and can be mitigated by controlling the potential to prevent excessive H coverage on the surface.

Having extensively explored potential deactivation pathways, we conclude that the system would be stranded in a thermodynamically metastable regime, undergoing significant hopping dynamics of center  $B^*H$ . The aggregation of extra boron content or borane formation, despite being more thermodynamically favorable under high H coverage, are kinetically hindered. This insight prompts us to reconsider our sampling approach in the previous section. By design, global optimization gravitates toward the thermodynamically most stable region, potentially leading to insufficient sampling of high-lying metastable states in the case of  $B_{1/3}$ . To address this, we incorporated a similarity-based geometric constraint into the GCGA, biasing it away from regions corresponding to major reconstruction or borane formation (Supplementary Note S1). In total, 2,477 more unique catalyst states are sampled in this metastable region. The H adsorption free energies and notable structures are shown in Figure 4, which no longer has the unphysical "cliff" in  $\Delta G_H$ . After all center B turn into  $B^*H$ , the subsequent H adsorbates would all bind to the bridge site on the  $B_6$  units until saturation. Due to the higher density of center B, H binding on bridge sites is significantly weakened, reaching a  $\Delta G_H$  of approximately 0.1 eV at higher H coverages — comparable to that of Pd and Pt.

## Realistic factors and their impact on HER activity

We have demonstrated in previous sections that the B-enriched hexagonal face of  $MoB_2$  exhibits multiple unusual behaviors: multiple non-equivalent binding sites and modes; intricate coverage effects on energetics due to the covalent nature of the B sheet; kinetic trapping and off-equilibrium evolution in the metastable regime. These complexities motivate us to go beyond thermodynamic-based activity descriptors (e.g.  $|\Delta G_H|$ ) and mean-field micro-kinetic models and to consider the realistic factors into HER activity model.

We first aim to identify the HER-relevant H coverage for  $B_0$ ,  $B_{1/9}$ , and  $B_{1/3}$  phases and how they evolve in response to varying electrode potential. Grand canonical density functional theory (GC-DFT) calculations are conducted to obtain the potential-dependent

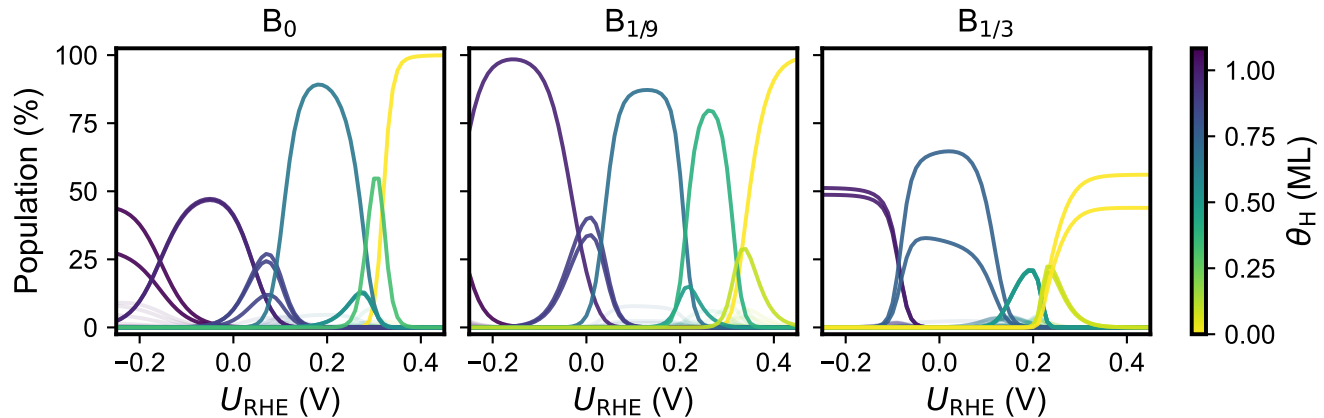


Figure 8: Evolution of H coverage on pristine and B-enriched hexagonal surfaces of  $\text{MoB}_2$ . The population of each coverage state is calculated based on potential dependent free energetics from grand canonical DFT calculations, assuming Boltzmann statistics.

electronic grand canonical free energy,  $\Omega_{\text{el}}$ , of all accessible surface states (details in Supplementary Note S3). We then also treat H adsorbate grand canonically, with respect to a potential-dependent chemical potential of H,  $\mu_{\text{H}}$ . This yields the total grand canonical free energy,  $\Omega_{\text{tot}}$ , which allows us to compare thermodynamic stability of catalysts states with different stoichiometry and under varying electrode potentials.

$$\Omega_{\text{tot}}(n_{\text{H}}, U) = \Omega_{\text{el}}^{n_{\text{H}}}(U) - \Omega_{\text{el}}^{\text{bare}}(U) - n_{\text{H}}\mu_{\text{H}} \quad (4)$$

Because the H adsorbate is found to be quite mobile over surface, with a low diffusion barrier of about 0.2 eV,(Supplementary Note S4) we assume that the adsorbate configuration can sufficiently equilibrate and obey Boltzmann statistics. The population of any catalyst state  $i$  at any given electrode potential  $U$  can then be evaluated by:

$$p_i(U) = \frac{e^{-\Omega_{\text{tot},i}(U)/k_{\text{B}}T}}{\sum_j^N e^{-\Omega_{\text{tot},j}(U)/k_{\text{B}}T}} \quad (5)$$

For the case of  $\text{B}_{1/3}$  phase, we only consider the sub-ensemble of unreconstructed states. This approximation allows us to compute the population of every catalyst state as a function of electrode potential (Figure 8). Across all three phases, significant underpotential deposi-

tion of hydrogen occurs, leading to H coverages exceeding 0.5 ML at the HER onset. The H coverage continue to increase as the potential sweeps to more negative until saturation. To avoid potential dissolution of surface B *via* borane formation, the over-potential should be kept below about 300 mV.

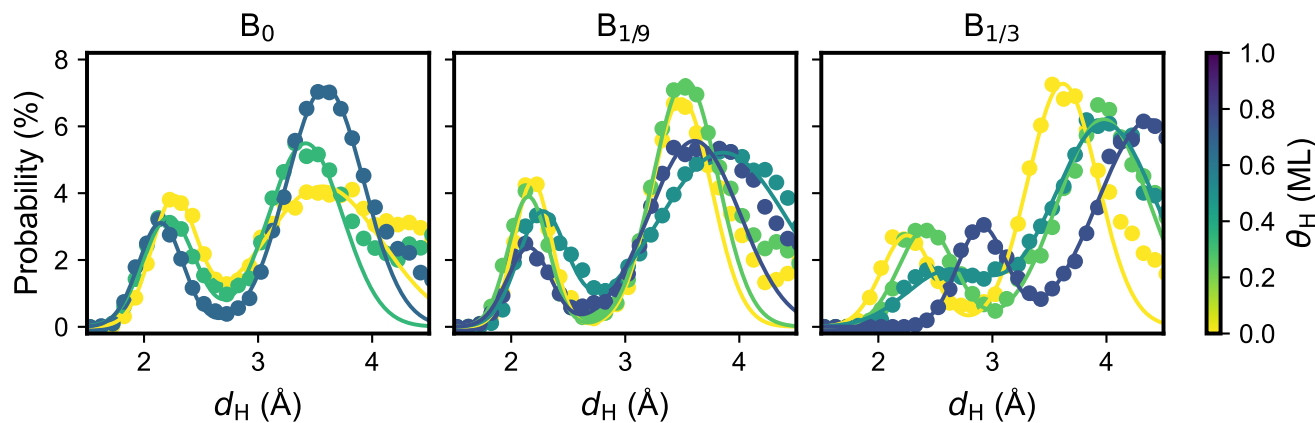


Figure 9: Distribution of the H–surface distance on pristine and B-enriched hexagonal surfaces of  $\text{MoB}_2$ . The circles are data points from *ab initio* molecular dynamics trajectories, and the curves are fitted to Gaussian density functions.

As H coverage varies within the HER-relevant potential window, the surface gradually transforms from a flat borophene-like configuration to a corrugated borophane-like one. Such variation in geometry and electronic structure shall induce different distribution of the solvent and electrolyte over the surface. To account for this, we perform *ab initio* molecular dynamics (AIMD) simulations with explicit water and hydronium for all three phases at different H coverage (Supplementary Note 5). Figure 9 shows the spatial distribution of hydronium H in the water/hydronium layer as a function of distance from pristine surface, with two apparent peaks represent the contact layer and the second water/hydronium layer. On  $\text{B}_0$  phase, the H in the contact layer gets closer to the surface as H coverage increases. This counter-intuitive trend is likely due to the attractive interaction between proton and the bridge H which has hydridic characters. On  $\text{B}_{1/9}$ , the adsorption of H on the center-atop site slightly repels the water layer away, which arises from the  $\sigma$  nature of the B-H bond (resembles the sterics of a typical C-H bond). On  $\text{B}_{1/3}$ , the repulsive effect of the center-atop H dominates the

surface-water/hydronium interaction. As H coverage increases, the B<sub>7</sub> units become more buckled, strengthening the structural corrugation within the sheet, pushing the center B\*H higher and the contact layer farther.

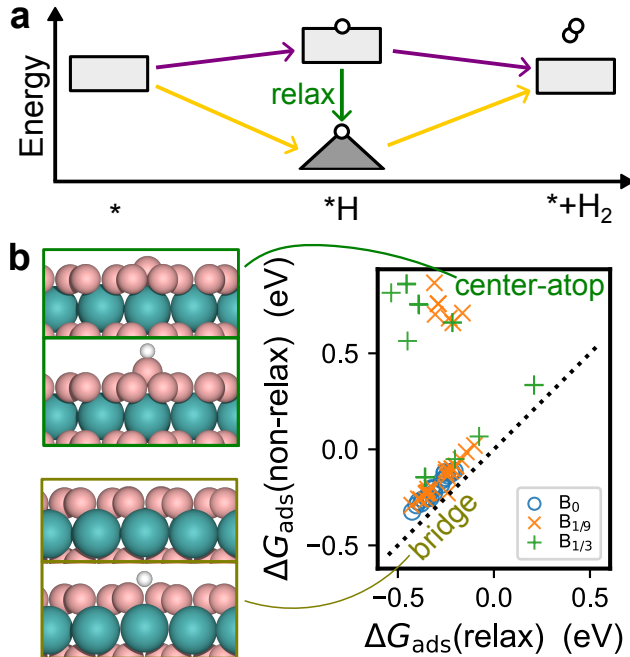


Figure 10: Site relaxation upon H adsorption and its consequences in energetics. (a) Schematic of adsorbate-induced site relaxation in the context of hydrogen evolution reaction. (b) Adsorption free energy of H on pristine and B-enriched hexagonal surfaces of MoB<sub>2</sub>, with or without structural relaxation of the site upon H adsorption. The two clusters of data points belong to center-atop and bridge sites, respectively, and the representative structures with and without H are shown next to the plot. Color code of atoms: Mo – blue, B – pink, H – white.

We then look into the role of the coverage-dependent corrugation of B<sub>7</sub> unit in HER kinetics. Figure 10a illustrates a typical energy diagram of HER steps. Upon adsorption, the active site needs to adapt its structure to better host the adsorbate. We can then decompose the binding energetics into two terms, the electronic interactions between the adsorbate and the site, and the energy associated with the structural relaxation of the site. The contribution from the latter is usually negligible for rigid surface such as surfaces of bulk metals or oxides, which is the basis of the success of linear scaling relations in those systems (pure electronic interactions on near-stationary sites). However, in the case of the

B-enriched MoB<sub>2</sub> surfaces, the contribution of the site relaxation is quite pronounced, akin to what is observed on subnanometer metal clusters.<sup>40</sup>

To quantify this effect, we consider two cases where the structure of a site is allowed or forbidden to relax upon H adsorption, resulting in two adsorption free energies,  $\Delta G_H(\text{relax})$  and  $\Delta G_H(\text{non-relax})$ , respectively. Figure 10 is a parity plot of the two energies on various sites of the accessible catalysts states of the B-enriched phases, under different H coverage. The distribution of  $\Delta G_H(\text{relax})$  of the bridge and center-atop sites are quite similar, both located around -0.3 eV. However, their  $\Delta G_H(\text{non-relax})$  behave very differently. For the bridge site, forbidding relaxation results in only a minor weakening of H binding (by less than 0.05 eV), indicating negligible structural changes upon adsorption. For the center-atop site, however, forbidding relaxation weakens H binding significantly—by about 1 eV. When relaxation is allowed, the center B atom elevates by approximately 0.5 Å upon H binding.

This stark difference in site relaxation energy arises from the distinct chemical bonding nature of the bridge and center-atop adsorption modes. The bridge site binds H *via* the 3c – 2e mode, with a bonding orbital that is resembles to a B-B  $\pi$  bonding orbital in spatial distribution. As a result, the site undergoes minimal change in structure and electron density to accommodate the H adsorbate (Figure S5). In contrast, the center-atop site binds H *via* the  $\sigma$  mode, which requires the center B to free up its  $p_z$  electrons. This leads to significant electron redistribution between the center B and its host B<sub>6</sub> (Figure S6 and Figure S5), weakening the B–B bonds and causing the center B to partially detach and pop up.

The surprisingly high energy contribution from site relaxation further prompts us to consider its implications on reaction kinetics. If site relaxation occurs significantly faster than the reaction steps, we can assume that the adsorption configuration always sufficiently relaxes to its minimum energy structure. Conversely, if site relaxation is significantly slower than the reaction steps, the site structure would remain near-stationary, with reaction steps proceeding in a vertical manner. Alternatively, if the timescales of the two processes are comparable, there may be some coupling between site relaxation and the reaction steps.

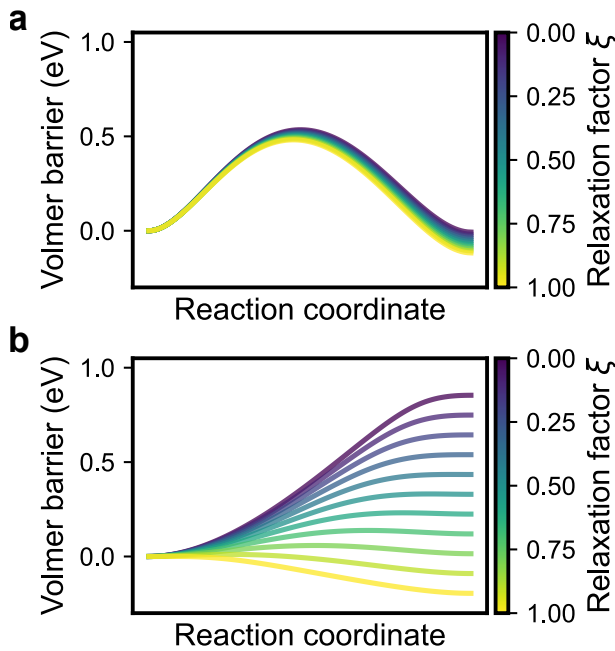


Figure 11: The impact of site relaxation on Volmer energetics on different sites. The free energy profiles at different relaxation factors of (a) bridge site and (b) center-atop site.

To better investigate the potential coupling effect, we introduce a relaxation factor,  $\xi$ , which describes the coupling between the site relaxation and the adsorption process, with values of 0 and 1 representing the fully relaxed and non-relaxed scenarios, respectively. The free energy profiles of a proton-coupled electron transfer (PCET) step can be computed using the analytical adiabatic model proposed in ref<sup>41</sup> (details in Supplementary Note S6).

$$V_{\text{PCET}} = \frac{V_{11} - V_{22}}{2} - \sqrt{\left| \frac{V_{11} - V_{22}}{2} \right| + V_{12}V_{21}} \quad (6)$$

Where  $V$  terms are the free energy surfaces (FESs) with 1 and 2 representing the surface and solvent sides, respectively. The decoupled potential on the solvent side,  $V_{11}$  and  $V_{22}$ , can be approximated by Morse type potentials:

$$V_{ii} = D_{e,i} - D_{e,i}(1 - \exp[-a_i(r - r_{\text{eq},i})])^2 = D_{e,i}(1 - \gamma_i) \quad (7)$$

where  $\gamma$  measures the electronic coupling strength. Due to the effect of surface site relaxation,

the decoupled potential on the surface side,  $V_{11}$ , has its parameters modified by  $\xi$ :

$$D_{e,1} = \xi D_{e,1}^{\text{relax}} + (1 - \xi) D_{e,1}^{\text{non-relax}} \quad (8)$$

$$a_1 = \xi a_1^{\text{relax}} + (1 - \xi) a_1^{\text{non-relax}} \quad (9)$$

$$r_{eq,1} = \xi r_{eq,1}^{\text{relax}} + (1 - \xi) r_{eq,1}^{\text{non-relax}} \quad (10)$$

The  $V_{12}$  and  $V_{21}$  terms, arising from the interaction between the donor and acceptor FESs, can then be written as:

$$V_{12} = V_{21} = \sqrt{\gamma_1(1 - \gamma_2)\gamma_2(1 - \gamma_1)D_{e,1}D_{e,2}} \quad (11)$$

which is also dependent on  $\xi$ . Plugging the  $V_{ij}$  terms back into Equation 6 yields the final PES of the PCET process.

We then apply this model to a bridge site and a center-atop site as representatives of the two H binding modes. The Volmer profile on the bridge site responds minimally to changes in  $\xi$ , with both the reaction energy and barrier remaining nearly identical (Figure 11a). However, the Volmer profile on the center-atop site changes dramatically as  $\xi$  varies, with both the reaction energy and barrier increasing by more than 1 eV, effectively converting it from an over-binding to an under-binding site for H adsorption (Figure 11b).

This strong relaxation effect can also influence the reaction kinetics by altering the rate-determining step. In Figure 12a, we show the variation of Volmer and Heyrovsky barriers on bridge and center-atop sites in response to varying  $\xi$ . The bridge site, which over-binds H, has a consistent Volmer-limited kinetics at all values of  $\xi$ . The center-atop site, however, transitions from Volmer-limited to Heyrovsky-limited kinetics as  $\xi$  decreases from 1 to 0, as a result of its shift from over-binding to under-binding.

Note that we consider only the Volmer-Heyrovsky mechanism in the following, as the H adsorbates tend to avoid occupying adjacent sites (*vide supra*), making the initial configuration for the Tafel step unfavorable and resulting in prohibitively high barriers (Supplementary

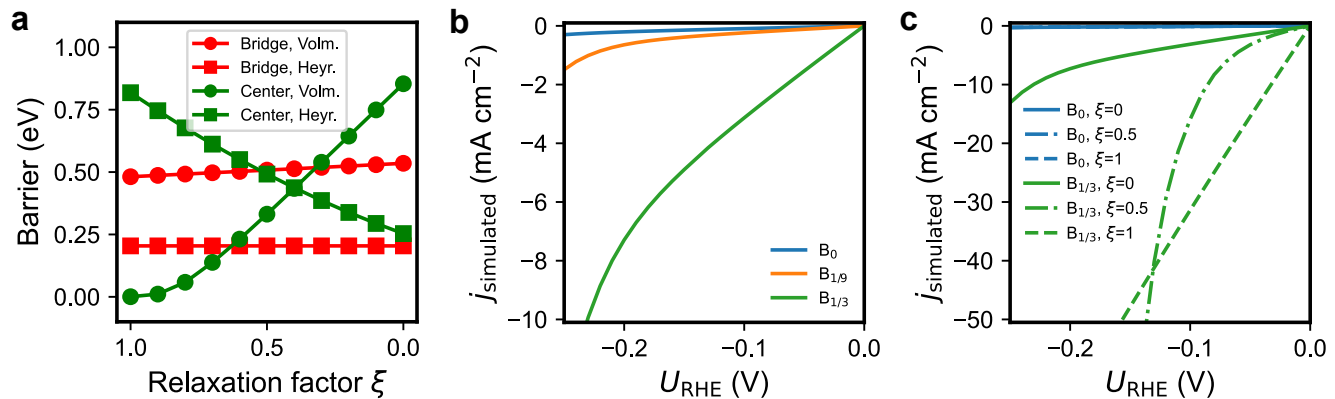


Figure 12: Hydrogen evolution reaction activity of pristine and B-enriched hexagonal surfaces of MoB<sub>2</sub>. (a) Response of Volmer and Heyrovsky barriers to varying relaxation factor on bridge and center-atop sites. (b) Simulated current density on B<sub>0</sub>, B<sub>1/9</sub>, and B<sub>1/3</sub> assuming no site relaxation, i.e.,  $\xi = 0$ . (c) Response of simulated current density to varying relaxation factor on B<sub>0</sub> and B<sub>1/3</sub> surfaces.

Note S7). This is further supported by the experimentally reported Tafel slope of approximately 50 mV/dec from previous studies,<sup>20</sup> which is characteristic of the Volmer-Heyrovsky mechanism.

We then build a non-mean-field model for the HER kinetics considering all afore discussed aspects, adapted from the models proposed in refs<sup>33,41,42</sup>. At a given potential  $U$ , we use Equation 5 to identify the accessible catalyst states and compute the ensemble-averaged H coverage  $\langle \theta_{\text{H}} \rangle$ :

$$\langle \theta_{\text{H}} \rangle = \sum_i p_i \theta_{\text{H},i}(U) \quad (12)$$

For each accessible catalyst state  $i$ , we construct the Volmer and Heyrovsky FESs (Supplementary Note S6) for every non-equivalent H adsorption site  $j$  using Equation 6, assuming the same  $\xi$  for all sites . The reaction rates on site  $j$  of catalyst state  $i$  can be computed from the barriers and then weighed by the probability distribution  $P_z$  in Figure 9:

$$r_{i,j} = \nu \int \langle \theta_{\text{site}}(U) \rangle P_z(\langle \theta_{\text{H}} \rangle, z) e^{-\Delta G_{i,j}^{\ddagger}(U, \xi, z)/k_{\text{B}}T} dz \quad (13)$$

where  $z$  is the distance between surface and H in water. We can sum up the rates over

every site for each catalyst state, and then weighed by the population of catalyst states in Figure 8, to obtain the final total rate:

$$r_{\text{tot}} = \sum_i p_i \left( \sum_j r_{i,j} \right) \quad (14)$$

Figure 12b shows the simulated HER current density at  $\xi = 0$ . We can see that B-enrichment of the surface greatly enhances HER activity. This is attributed to the corrugation of the  $B_7$  unit under H coverage, creating center BH sites that protrude and make closer contact with the water/hydronium layer, facilitating proton transfer kinetics. Compared to  $B_{1/9}$ ,  $B_{1/3}$  not only has a higher density of these center BH sites but also exhibits greater geometric corrugation due to increased strain within the sheet caused by the crowding of more B. Since a pristine hexagonal B layer is found to be inactive for HER, we suspect the experimentally reported high HER activity on  $\text{MoB}_2$  and its derivatives comes from extra boron content on the surface layer as remnants from synthetic conditions.

Next, we increase  $\xi$  and probe its impact on overall HER kinetics in Figure 12c. The  $B_0$  phase, which only offers bridge H sites, undergoes nearly no change in activity. The  $B_{1/3}$  phase, however, experiences a significant increase in HER activity at  $\xi = 1$ , because site relaxation shifts the H binding energetics from severely under-binding to slightly over-binding. Moreover, as seen in Figure 12a, there exists a specific  $\xi$  value that minimizes the overall barriers at the crossover point of the rate-determining steps. This is confirmed by the exceptionally high simulated HER activity at  $\xi = 0.5$ , surpassing those at  $\xi = 0$  or 1.

Note that  $\xi$  is likely dependent on the nature of the site, with its exact value unknown. For surfaces made of heavier elements such as metal facets, the timescale for relaxation should be significantly longer than adsorption processes. For light elements, the surface site should be able to relax partially during the adsorption event to an extent unknown.  $\xi$  should also depend on the nature of the adsorbate and the mechanism of the adsorption. PCET is typically very fast, but adsorption of heavier adsorbates such as O and CO can be

much slower. Ultimately,  $\xi$  depends on the local morphology of the FES defined by multiple factors. Since site relaxation solely can contribute up to 1 eV in adsorption energy, if we can find a way to control it even to a small extent, such as by external fields, it can potentially offer an alternative dimension of catalyst design.

## Conclusions

In this work, we propose a B-enriching strategy to tune the surface reactivity of the metal diborides. The arrangement of surface boron is dependent on H coverage, with strong kinetic trapping effect to retain to its initial configuration instead of drastically reconstruct or deactivate. The heterogeneity of surface sites from B-enriching, in geometry, adsorption energetics, and fluxionality, can also have profound implication on the kinetics of relatively fast reaction steps. We would like to emphasize the key role of off-equilibrium states and processes in catalysis, and how they can emerge in seemingly simple systems. These complexities can be addressed affordably using the generalizable computational workflow herein. The presented computational framework and the gained insights into off-equilibrium behaviors can be relevant to a wide range of catalyst and materials systems, providing a new perspective in computational understanding and design.

## Computational methods

The hexagonal face of molybdenum diboride (*P6/mmm*) is modeled by a 6-layer  $3 \times 3$  supercell of (001) termination with a surface area of 71.581 Å. The bottom 3 atomic layers of the slab is constrained as the bulk region, and all others are allowed to relax as the interface region. A vacuum slab of 15 Å is added in the *z* direction to avoid spurious interactions between periodic images (Figure S1).

The density functional theory (DFT) calculations are performed with the PBE functional<sup>43</sup> and PBE\_PAW pseudopotentials<sup>44,45</sup> (H, B, and Mo\_pv) using the VASP program

(version 5.4.4).<sup>46–49</sup> The D3 correction is added to better account for dispersion interactions.<sup>50</sup> The convergence criteria for electronic and force minimization are  $10^{-5}$  eV and  $2.0 \times 10^{-2}$  eV/Å, respectively. The Brillouin zone is sampled using Γ-centered  $2 \times 2 \times 1$   $k$ -points, and the kinetic energy cutoff for the plane-waves is 500 eV.

All electronic structure analyses are performed based on converged wavefunctions or charge densities. Electron localization functions are computed within VASP. Bader charges are computed using the Bader Charge Analysis program.<sup>51</sup> Quantum theory of atoms in molecules analysis are performed using the critic2 program.<sup>52</sup> Isosurfaces are visualized using the VESTA program.<sup>53</sup>

The global optimization minima searches are performed using our open-sourced *Python* package, **GOCIA**.<sup>54</sup> The structures of the hexagonal face with varying amount of surface boron is sampled with an adapted version of the bond length distribution algorithm (BLDA).<sup>55</sup> The structure of the  $B_0$ ,  $B_{1/9}$ , and  $B_{1/3}$  surface phases under varying H coverage is sampled with the grand canonical genetic algorithm (GCGA).<sup>35</sup> Additional similarity constraints (full details in Supplementary Note S1) are added to the sampling of unreconstructed  $B_{1/3}$  under varying H coverage.

Due to the complexity of the potential energy surface (PES) of center B migration, we construct their PES from relaxed 2-dimensional scan calculations (details in SI). The minimum energy paths (MEPs) are located on the corresponding PES using the string method (Supplementary Note S2).<sup>56</sup> The transition states of simpler processes, such as H diffusion, are located using the nudged elastic band method.<sup>57</sup>

The GC-DFT calculations are performed using the surface charging method<sup>58</sup> implemented in **GOCIA**, with details in Supplementary Note S3. Only the structures within 0.2 eV from the GM of their corresponding stoichiometry are considered.

*Ab initio* molecular dynamics simulations are performed using the same DFT methods as mentioned, except for a lower kinetic energy cutoff of 400 eV. The simulations are performed within the *NVT* ensemble at 300 K with a Nosé-Hoover thermostat.<sup>59,60</sup> The simulations

are run with a time step of 1 fs, and a 10 ps trajectory is collected after pre-equilibration for analysis. Full details are in Supplementary Note S5.

## Data Availability

All minima structures from the grand canonical global optimization minima searches are available on the catalysis-hub.org repository.<sup>61</sup>

## Acknowledgement

Z.Z. is supported by the Stanford Energy Fellowship from the Precourt Institute of Energy, Doerr School of Sustainability. F.A-P. acknowledges support from the U.S. Department of Energy, Office of Science, Office of Basic Energy Sciences, Chemical Sciences, Geosciences, and Biosciences Division, Catalysis Science Program to the SUNCAT Center for Interface Science and Catalysis. Computational facilities used to conduct this study include: S3DF, SLAC Shared Scientific Data Facility; Sherlock, a university-shared computing cluster operated by Stanford Research Computing Center; National Energy Research Scientific Computing Center, a DOE Office of Science User Facility supported by the Office of Science of the U.S. Department of Energy under Contract No. DE-AC02-05CH11231 using NERSC award BES-ERCAP0024127. Z.Z. thanks Thomas F. Jaramillo, Michal Bajdich, and Kirsten Winther for helpful discussions and assistance in uploading datasets to Catalysis-Hub.

## Supporting Information Available

The Supporting Information is available free of charge at xxxxx:

Slab models for the GCGA, GC-DFT, and AIMD simulations; Pourbaix diagram of boron in aqueous media; Bader charge analyses; Electron localization function analyses; Charge density difference analysis; Quantum theory of atoms in molecules analyses; Global

and minima structures from global optimization searches; Progress plot of GCGA searches; Similarity map of sampled H-covered  $B_{1/3}$  structures from GCGA searches; Surface atom corrugation under varying H coverage; Population of different H binding sites and modes under varying H coverage; Energy profiles of in-plane B rearrangement, H diffusion, and Tafel step from NEB calculations; PES of center B/B\*H migration, dimerization, trimerization, and borane formation from 2D PES scans; Key AIMD snapshots showing delocalization of proton in hydronium/water layers and micro-solvation clusters; Fitting of decoupled PES to Morse potentials; Combined adiabatic FES of PCET and its response to varying  $U_{\text{RHE}}$  and  $\xi$ ; Note on details of the GC global optimizations; Note on PES and MEP samplings; Note on GC-DFT calculations; Note on kinetics of H diffusion among surface sites; Note on AIMD simulations; Note on electrochemical barriers from decoupled PESs; Note on kinetics of the Tafel step under relevant H coverage.

## References

- (1) Welch, A. J. The significance and impact of Wade's rules. *Chemical Communications* **2013**, *49*, 3615–3616.
- (2) Zubarev, D. Y.; Boldyrev, A. I. " Developing paradigms of chemical bonding: adaptive natural density partitioning. *Physical chemistry chemical physics* **2008**, *10*, 5207–5217.
- (3) Mannix, A. J.; Zhang, Z.; Guisinger, N. P.; Yakobson, B. I.; Hersam, M. C. Borophene as a prototype for synthetic 2D materials development. *Nature nanotechnology* **2018**, *13*, 444–450.
- (4) Chen, C.; Lv, H.; Zhang, P.; Zhuo, Z.; Wang, Y.; Ma, C.; Li, W.; Wang, X.; Feng, B.; Cheng, P.; others Synthesis of bilayer borophene. *Nature Chemistry* **2022**, *14*, 25–31.
- (5) Zhou, X.-F.; Oganov, A. R.; Shao, X.; Zhu, Q.; Wang, H.-T. Unexpected reconstruction of the  $\alpha$ -boron (111) surface. *Physical Review Letters* **2014**, *113*, 176101.

- (6) Alexandrova, A. N.; Boldyrev, A. I.; Zhai, H.-J.; Wang, L.-S. All-boron aromatic clusters as potential new inorganic ligands and building blocks in chemistry. *Coordination Chemistry Reviews* **2006**, *250*, 2811–2866.
- (7) Li, W.-L.; Chen, X.; Jian, T.; Chen, T.-T.; Li, J.; Wang, L.-S. From planar boron clusters to borophenes and metalloborophenes. *Nature Reviews Chemistry* **2017**, *1*, 0071.
- (8) Wang, L.-S. Borozenes: Benzene-like planar aromatic boron clusters. *Accounts of Chemical Research* **2024**, *57*, 2428–2436.
- (9) Oganov, A.; Solozhenko, V. Boron: a hunt for superhard polymorphs. *Journal of Superhard Materials* **2009**, *31*, 285–291.
- (10) Pangilinan, L. E.; Hu, S.; Hamilton, S. G.; Tolbert, S. H.; Kaner, R. B. Hardening effects in superhard transition-metal borides. *Accounts of Materials Research* **2021**, *3*, 100–109.
- (11) Kortus, J.; Mazin, I.; Belashchenko, K. D.; Antropov, V. P.; Boyer, L. Superconductivity of metallic boron in MgB<sub>2</sub>. *Physical Review Letters* **2001**, *86*, 4656.
- (12) Scheifers, J. P.; Zhang, Y.; Fokwa, B. P. Boron: enabling exciting metal-rich structures and magnetic properties. *Accounts of chemical research* **2017**, *50*, 2317–2325.
- (13) Zhang, J.; Liu, J.; Liao, H.; Zeng, M.; Ma, S. A review on relationship between morphology of boride of Fe-B alloys and the wear/corrosion resistant properties and mechanisms. *Journal of Materials Research and Technology* **2019**, *8*, 6308–6320.
- (14) Saglik, K.; Mete, B.; Terzi, I.; Candolfi, C.; Aydemir, U. Thermoelectric borides: Review and future perspectives. *Advanced Physics Research* **2023**, *2*, 2300010.
- (15) Jothi, P. R.; Yubuta, K.; Fokwa, B. P. A simple, general synthetic route toward nanoscale transition metal borides. *Advanced Materials* **2018**, *30*, 1704181.

- (16) Portehault, D.; Devi, S.; Beaunier, P.; Gervais, C.; Giordano, C.; Sanchez, C.; Antonietti, M. A general solution route toward metal boride nanocrystals. *Angewandte Chemie-German Edition* **2011**, *123*, 3320.
- (17) Hong, J.; Mutalik, S.; Pescarmona, P. P.; Protesescu, L. Metal Borides: From Industrial Classics to Versatile Colloidal Nanocrystals for Energy, Catalysis, and Hard Coatings Applications. *Chemistry of Materials* **2024**, *36*, 2147–2164.
- (18) Gupta, S.; Patel, M. K.; Miotello, A.; Patel, N. Metal boride-based catalysts for electrochemical water-splitting: A review. *Advanced Functional Materials* **2020**, *30*, 1906481.
- (19) Kawashima, K.; Márquez, R. A.; Smith, L. A.; Vaidyula, R. R.; Carrasco-Jaim, O. A.; Wang, Z.; Son, Y. J.; Cao, C. L.; Mullins, C. B. A review of transition metal boride, carbide, pnictide, and chalcogenide water oxidation electrocatalysts. *Chemical Reviews* **2023**, *123*, 12795–13208.
- (20) Lee, E.; Fokwa, B. P. Nonprecious metal borides: Emerging electrocatalysts for hydrogen production. *Accounts of Chemical Research* **2021**, *55*, 56–64.
- (21) Park, H.; Encinas, A.; Scheifers, J. P.; Zhang, Y.; Fokwa, B. P. Boron-dependency of molybdenum boride electrocatalysts for the hydrogen evolution reaction. *Angewandte Chemie International Edition* **2017**, *56*, 5575–5578.
- (22) Park, H.; Zhang, Y.; Scheifers, J. P.; Jothi, P. R.; Encinas, A.; Fokwa, B. P. Graphene- and phosphorene-like boron layers with contrasting activities in highly active Mo<sub>2</sub>B<sub>4</sub> for hydrogen evolution. *Journal of the American Chemical Society* **2017**, *139*, 12915–12918.
- (23) Li, S.; Gunda, H.; Ray, K. G.; Wong, C.-S.; Xiao, P.; Friddle, R. W.; Liu, Y.-S.; Kang, S.; Dun, C.; Sugar, J. D.; others Spontaneous dynamical disordering of borophenes in MgB<sub>2</sub> and related metal borides. *Nature Communications* **2021**, *12*, 6268.

- (24) Venegas, J. M.; McDermott, W. P.; Hermans, I. Serendipity in catalysis research: boron-based materials for alkane oxidative dehydrogenation. *Accounts of chemical research* **2018**, *51*, 2556–2564.
- (25) Zhang, Z.; Jimenez-Izal, E.; Hermans, I.; Alexandrova, A. N. Dynamic phase diagram of catalytic surface of hexagonal boron nitride under conditions of oxidative dehydrogenation of propane. *The journal of physical chemistry letters* **2018**, *10*, 20–25.
- (26) Cendejas, M. C.; Paredes Mellone, O. A.; Kurumbail, U.; Zhang, Z.; Jansen, J. H.; Ibrahim, F.; Dong, S.; Vinson, J.; Alexandrova, A. N.; Sokaras, D.; others Tracking Active Phase Behavior on Boron Nitride during the Oxidative Dehydrogenation of Propane Using Operando X-Ray Raman Spectroscopy. *Journal of the American Chemical Society* **2023**, *145*, 25686–25694.
- (27) Zhang, Z.; Hermans, I.; Alexandrova, A. N. Off-stoichiometric Restructuring and Sliding Dynamics of Hexagonal Boron Nitride Edges in Conditions of Oxidative Dehydrogenation of Propane. *Journal of the American Chemical Society* **2023**, *145*, 17265–17273.
- (28) Venegas, J. M.; Zhang, Z.; Agbi, T. O.; McDermott, W. P.; Alexandrova, A.; Hermans, I. Why boron nitride is such a selective catalyst for the oxidative dehydrogenation of propane. *Angewandte Chemie International Edition* **2020**, *59*, 16527–16535.
- (29) Nishino, H.; Fujita, T.; Cuong, N. T.; Tominaka, S.; Miyauchi, M.; Iimura, S.; Hirata, A.; Umezawa, N.; Okada, S.; Nishibori, E.; others Formation and characterization of hydrogen boride sheets derived from MgB<sub>2</sub> by cation exchange. *Journal of the American Chemical Society* **2017**, *139*, 13761–13769.
- (30) Li, Q.; Kolluru, V. S. C.; Rahn, M. S.; Schwenker, E.; Li, S.; Hennig, R. G.; Darancet, P.; Chan, M. K.; Hersam, M. C. Synthesis of borophane polymorphs through hydrogenation of borophene. *Science* **2021**, *371*, 1143–1148.

- (31) Kawamura, R.; Cuong, N. T.; Fujita, T.; Ishibiki, R.; Hirabayashi, T.; Yamaguchi, A.; Matsuda, I.; Okada, S.; Kondo, T.; Miyauchi, M. Photoinduced hydrogen release from hydrogen boride sheets. *Nature communications* **2019**, *10*, 4880.
- (32) Rojas, K. I. M.; Cuong, N. T.; Nishino, H.; Ishibiki, R.; Ito, S.-i.; Miyauchi, M.; Fujimoto, Y.; Tominaka, S.; Okada, S.; Hosono, H.; others Chemical stability of hydrogen boride nanosheets in water. *Communications Materials* **2021**, *2*, 81.
- (33) Zhang, Z.; Cui, Z.-H.; Jimenez-Izal, E.; Sautet, P.; Alexandrova, A. N. Hydrogen evolution on restructured B-rich WB: metastable surface states and isolated active sites. *ACS Catalysis* **2020**, *10*, 13867–13877.
- (34) Weng, X.-J.; Bai, J.; Hou, J.; Zhu, Y.; Wang, L.; Li, P.; Nie, A.; Xu, B.; Zhou, X.-F.; Tian, Y. Experimental evidence of surface copper boride. *Nano Research* **2023**, *16*, 9602–9607.
- (35) Zhang, Z.; Wei, Z.; Sautet, P.; Alexandrova, A. N. Hydrogen-Induced Restructuring of a Cu(100) Electrode in Electroreduction Conditions. *Journal of the American Chemical Society* **2022**, *144*, 19284–19293.
- (36) Zhang, Z.; Gee, W.; Sautet, P.; Alexandrova, A. N. H and CO Co-Induced Roughening of Cu Surface in CO<sub>2</sub> Electroreduction Conditions. *Journal of the American Chemical Society* **2024**,
- (37) Shah, A. H.; Zhang, Z.; Wan, C.; Wang, S.; Zhang, A.; Wang, L.; Alexandrova, A. N.; Huang, Y.; Duan, X. Platinum Surface Water Orientation Dictates Hydrogen Evolution Reaction Kinetics in Alkaline Media. *Journal of the American Chemical Society* **2024**, *146*, 9623–9630.
- (38) Zhang, Z.; Li, J.; Wang, Y.-G. Modeling Interfacial Dynamics on Single Atom Electrocatalysts: Explicit Solvation and Potential Dependence. *Accounts of Chemical Research* **2024**, *57*, 198–207.

- (39) Nørskov, J. K.; Bligaard, T.; Logadottir, A.; Kitchin, J.; Chen, J. G.; Pandelov, S.; Stimming, U. Trends in the exchange current for hydrogen evolution. *Journal of The Electrochemical Society* **2005**, *152*, J23.
- (40) Yan, G.; Vlachos, D. G. Impact of Metal Clusters on the Lewis Acidity of Oxide Surfaces: First-Principles Calculations of Pt10/ $\gamma$ -Al<sub>2</sub>O<sub>3</sub> (110). *The Journal of Physical Chemistry C* **2024**, *128*, 16996–17005.
- (41) Li, J.; Stenlid, J. H.; Ludwig, T.; Lamoureux, P. S.; Abild-Pedersen, F. Modeling potential-dependent electrochemical activation barriers: revisiting the alkaline hydrogen evolution reaction. *Journal of the American Chemical Society* **2021**, *143*, 19341–19355.
- (42) Zhang, Z.; Masubuchi, T.; Sautet, P.; Anderson, S. L.; Alexandrova, A. N. Hydrogen Evolution on Electrode-Supported Ptn Clusters: Ensemble of Hydride States Governs the Size Dependent Reactivity. *Angewandte Chemie* **2023**, *135*, e202218210.
- (43) Perdew, J. P.; Burke, K.; Ernzerhof, M. Generalized gradient approximation made simple. *Physical review letters* **1996**, *77*, 3865.
- (44) Kresse, G.; Joubert, D. From ultrasoft pseudopotentials to the projector augmented-wave method. *Physical review b* **1999**, *59*, 1758.
- (45) Blöchl, P. E. Projector augmented-wave method. *Physical review B* **1994**, *50*, 17953.
- (46) Kresse, G.; Hafner, J. Ab initio molecular dynamics for liquid metals. *Physical Review B* **1993**, *47*, 558–561.
- (47) Kresse, G.; Hafner, J. Ab initio molecular-dynamics simulation of the liquid-metal–amorphous-semiconductor transition in germanium. *Physical Review B* **1994**, *49*, 14251–14269.

- (48) Kresse, G.; Furthmüller, J. Efficient iterative schemes for ab initio total-energy calculations using a plane-wave basis set. *Physical Review B* **1996**, *54*, 11169–11186.
- (49) Kresse, G.; Furthmüller, J. Efficiency of ab-initio total energy calculations for metals and semiconductors using a plane-wave basis set. *Computational Materials Science* **1996**, *6*, 15–50.
- (50) Grimme, S.; Antony, J.; Ehrlich, S.; Krieg, H. A consistent and accurate ab initio parametrization of density functional dispersion correction (DFT-D) for the 94 elements H-Pu. *The Journal of chemical physics* **2010**, *132*.
- (51) Yu, M.; Trinkle, D. R. Accurate and efficient algorithm for Bader charge integration. *The Journal of chemical physics* **2011**, *134*.
- (52) Otero-de-la Roza, A.; Johnson, E. R.; Luaña, V. Critic2: A program for real-space analysis of quantum chemical interactions in solids. *Computer Physics Communications* **2014**, *185*, 1007–1018.
- (53) Momma, K.; Izumi, F. VESTA 3 for three-dimensional visualization of crystal, volumetric and morphology data. *Applied Crystallography* **2011**, *44*, 1272–1276.
- (54) Zhang, Z.; Gee, W.; Lavroff, R. H.; Alexandrova, A. N. GOCIA: a grand canonical global optimizer for clusters, interfaces, and adsorbates. *Physical Chemistry Chemical Physics* **2025**, *27*, 696–706.
- (55) Zhai, H.; Alexandrova, A. N. Local fluxionality of surface-deposited cluster catalysts: The case of Pt7 on Al<sub>2</sub>O<sub>3</sub>. *The journal of physical chemistry letters* **2018**, *9*, 1696–1702.
- (56) Weinan, E.; Ren, W.; Vanden-Eijnden, E. String method for the study of rare events. *Physical Review B* **2002**, *66*, 052301.
- (57) Mills, G.; Jónsson, H.; Schenter, G. K. Reversible work transition state theory: application to dissociative adsorption of hydrogen. *Surface Science* **1995**, *324*, 305–337.

- (58) Steinmann, S. N.; Sautet, P. Assessing a First-Principles Model of an Electrochemical Interface by Comparison with Experiment. *Journal of Physical Chemistry C* **2016**, *120*, 5619–5623.
- (59) Shuichi, N. Constant temperature molecular dynamics methods. *Progress of Theoretical Physics Supplement* **1991**, *103*, 1–46.
- (60) Hoover, W. G. Canonical dynamics: Equilibrium phase-space distributions. *Physical review A* **1985**, *31*, 1695.
- (61) Winther, K. T.; Hoffmann, M. J.; Boes, J. R.; Mamun, O.; Bajdich, M.; Bligaard, T. Catalysis-Hub. org, an open electronic structure database for surface reactions. *Scientific data* **2019**, *6*, 75.

# TOC Graphic

